PERGAMON

International Journal of Heat and Mass Transfer 45 (2002) 4761–4771

International Journal of HEAT and MASS TRANSFER

www.elsevier.com/locate/ijhmt

High-speed visualization of boiling from an enhanced structure

C. Ramaswamy [a], Y. Joshi [b,*], W. Nakayama [c], W.B. Johnson [d]

[a] *IBM Corporation, Hopewell Junction, NY 12533, USA*
[b] *G.W. Woodruff School of Mechanical Engineering, Georgia Institute of Technology, Atlanta, GA 30332, USA*
[c] *ThermTech International, Kanagawa, 255-0004, Japan*
[d] *Laboratory for Physical Sciences, College Park, MD 20740, USA*

Received 14 January 2002; received in revised form 16 May 2002

Abstract

Using high-speed photography (1500 frames/s) bubble growth data on microporous structures immersed in a pool of dielectric coolant (FC-72) were obtained. Wafer dicing and wet etching was used to fabricate a net of interconnected microchannels on a 10 mm × 10 mm piece of silicon wafer. The resultant structure has pores that communicate the interior of microchannels to the liquid pool. The pore diameter was varied in a range 0.12–0.20 mm and the pore pitch in 0.7–1.4 mm. The data were collected maintaining the system pressure at one atmosphere and increasing the wall superheat up to 12 K.

Among the geometrical parameters, the pore diameter was found to be most influential on the bubble departure diameter. The findings about the bubble growth rate, the bubbling frequency, and the bubble site density were largely in accord with the previously reported data. However, the coverage of wider ranges of wall superheat and the structural parameters in the present study revealed new bubble characteristics that was used in implementing an analytical model for boiling heat transfer on the porous structure.

1. Introduction

The mechanism of pool boiling is a complex one with several factors contributing to the high heat transfer rates. These include latent heat transfer, natural convection, microconvection and Marangoni flow. Several investigators have used high-speed visualization as a tool to quantify the relative contribution of the above mentioned components. For example, Han and Griffith [1] used high-speed photography (2400 frames/s) to study boiling from a cylindrical copper block (30.2 mm diameter) plated with a 0.125 mm layer of gold, with distilled water as the working fluid. They measured the bubble departure diameters and frequency of bubble generation to predict the latent heat flux. Paul and Abdel-Khalik [2] carried out visualization of boiling from a platinum wire, 0.3 mm in diameter and 30 mm long, with distilled water as the working fluid. Using a high-speed movie camera (6400 frames/s) the departure diameter, frequency and nucleation site density was measured. The data showed that latent heat was the dominant mechanism of heat transfer in the nucleate boiling regime. The study also showed that the bubble departure diameter, frequency and nucleation site density, for a particular heat flux value, could be represented by statistical functions. Recently, Ammerman and You [3] developed a single-photo/laser doppler anemometry (LDA) technique to investigate the volumetric vapor flow from a heated platinum wire in FC-72. A random set of five frames was chosen at each heat flux level and the volumetric flow rate determined within an area of interest. Combined with the measurements of the LDA, the average bubble diameter was computed. Their analysis confirmed that latent heat transport was the dominant mechanism in nucleate boiling.

Investigators have also used high-speed visualization for qualitative analysis of the boiling mechanism. Sun and Lienhard [4] carried out high-speed visualization, using a movie camera, on nichrome wires 101.6 mm in

* Corresponding author. Tel.: +1-404-385-2810; fax: +1-404-894-8496.
E-mail address: yogendra.joshi@me.gatech.edu (Y. Joshi).

0017-9310/02/$ - see front matter © 2002 Elsevier Science Ltd. All rights reserved.
PII: S0017-9310(02)00196-5

Nomenclature

B	width of the enhanced structure (mm)	t	time (s)
D	instantaneous bubble diameter (mm)	Δt_g	growth period for an individual bubble (s)
D_d	bubble departure diameter (mm)	Δt_w	waiting time for bubble initiation (s)
f	frequency (Hz)	T_{sat}	saturation temperature of FC-72 (°C)
g	acceleration due to gravity (9.81 m/s^2)	T_{wall}	temperature at the bottom of the enhanced structures (°C)
H_t	channel depth (mm)	ΔT_{sup}	wall superheat ($T_{wall} - T_{sat}$), (°C)
H_s	height of the enhanced structure (mm)	W_t	channel width—also pore size (mm)
L	length of the enhanced structure (mm)		
P_t	channel pitch—also pore pitch (mm)		

length and diameter in the range 0.125–2 mm. Four different organic liquids: acetone, methanol, benzene and isopropanol were used. The emphasis of the study was to understand the vapor and liquid interaction at critical heat flux. A correlation was derived to predict the thickness of the vapor blanket layer for this state. Katto and Yakoya [5] studied the boiling of saturated water at one atmosphere from a horizontal, 10 mm diameter, heated disc. They found that the vapor mass above the heated surface can be classified into three categories depending on the influence between consecutive bubbles. In the first category, consecutive vapor masses are independent of each other. In the second, the growing vapor mass is almost attached to the preceding one and is much smaller in size. The final category consists of vapor masses that are separated from the preceding one but grow under the influence of the flow generated by the preceding one and are almost columnar in shape.

The above mentioned studies and similar ones in literature are mostly for plain polished surfaces only. There is sufficient evidence in literature demonstrating the very high heat transfer rates (~100 W/cm^2) achievable with enhanced surfaces (see Webb [6]). However, studies on understanding the mechanism of boiling from these surfaces are limited. Nakayama et al. [7–9] were among the first to carry out visualization of the boiling process from a structured surface. The surface consisted of a rectangular channel covered with a thin sheet that had pores at a regular pitch (Fig. 1) and the entire structure was immersed in R-11. They used a laser probe to measure the frequency of bubble formation and the population density of the bubbles. They found that liquid in the channel evaporated to form vapor regions, which were then ejected as bubbles from the pores. As the bubbles ejected, liquid filled into the channels through the pores and spread axially along thin menisci along the sharp corners of the channel. With addition of heat, the frequency of bubbles and the number of bubbles increased, but the basic phenomenon remained the same. An analytical model was formulated to predict a few of these parameters.

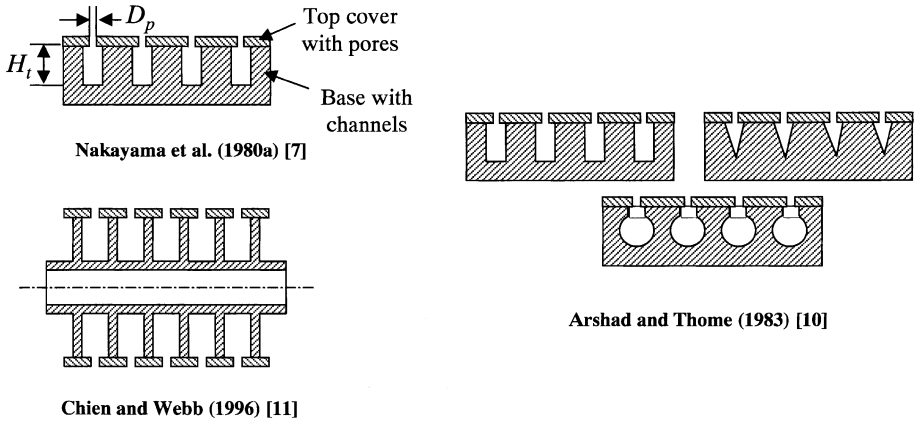

Fig. 1. Cross-sectional view of structures used by authors for boiling visualization.

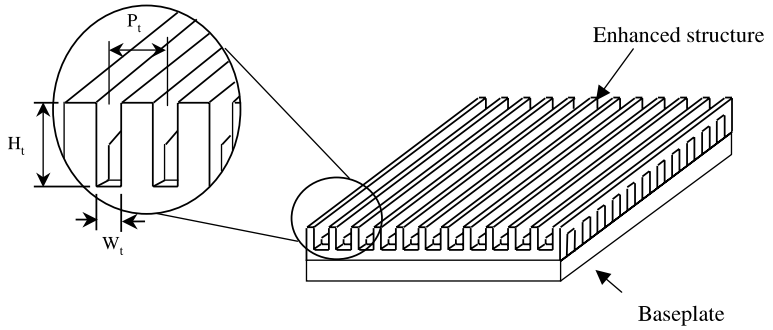

Fig. 2. Enhanced structures employed in this study.

Arshad and Thome [10] conducted flow visualization from similar surfaces (Fig. 1) to understand the mechanism of boiling inside the channels. This study confirmed that the primary mechanism of heat transfer inside the channels was evaporation of the thin liquid menisci in sharp corners. The study also showed that the vapor initiation was from one of the sharp corners and quickly spread to occupy a large portion of the channel volume. The vapor was then ejected in the form of bubbles from the surface pores. Recently, Chien and Webb [11] conducted high-speed visualization (1000 frames/s) of boiling in R-123 from a finned-tube which was covered with a thin sheet and had pores at regular intervals (Fig. 1). The bubble departure diameter, frequency of bubble formation and the bubble site density were measured. The bubble growth data showed bubbles departing at a faster rate compared to those on a plain surface. The study concluded that the bubble formation phenomenon was thus different than that on a plain polished surface. The bubble data were used to develop a semi-analytical model for the boiling process.

The above mentioned studies [7–11] on structured surfaces have been carried out for a limited range of wall superheat (0–4 °C). With fluorinert liquids (e.g. FC-72), wall superheats as high as 30 °C can be reached in applications such as electronic cooling, with the wall temperature below 85 °C. Hence studies for a wider range of wall superheats are required to understand the boiling mechanism with these liquids. The current study involves visualization of boiling from one such enhanced structure in the wall superheat range 4–30 °C. The enhanced structure consists of an array of channels and pores that make the structure highly porous. Details of this structure are presented in the next section. The parameters measured were bubble diameter as a function of time, departure diameter, frequency of bubble formation and the bubble site density (nucleation density). The ultimate goal was to use the data for formulating a semi-analytical model that predicts the heat transfer performance of these structures. A framework for developing such a model has been outlined using a flowchart and sample results are included.

2. Enhanced structures

The enhanced structure, which was the focus of this study, is shown in Fig. 2 and its construction is similar to the one studied by Nakayama et al. [12]. The structures have an array of rectangular channels cut on either side of a 10 mm × 10 mm silicon substrate and aligned at an angle of 90° to each other. The depth of the channels is more than half the thickness of the substrate, resulting in the channels intersecting at discrete locations to provide square pores. In this study, silicon substrates were used to fabricate the enhanced structures. The advantage of using silicon is that the enhanced structures can be directly bonded to the passive side of a heat dissipating silicon chip, resulting in significantly lower thermal resistance and eliminating coefficient of thermal expansion (CTE) mismatch.

Two methods of microfabrication, compatible with chip manufacturing, were used for silicon—wet etching and wafer dicing. In wet etching, a silicon wafer with $\langle 1\,1\,0 \rangle$ crystal orientation was patterned using photolithography and then etched using a 40% KOH solution. In this technique, the channel walls are defined by the orientation of $\langle 1\,1\,1 \rangle$ crystal planes. These planes are aligned at an angle of 109.53° and hence the pores are trapezoidal in shape (Fig. 3a).

In wafer dicing, a high-speed saw, with diamond impregnated nickel blades, was used to mill the channels one at a time. The width of the channels was varied using blades of different thickness. This resulted in pores of different sizes. Since this technique is independent of the crystal orientation, the channels were orthogonal resulting in square pores (Fig. 3b). The structures thus fabricated were then bonded to a silicon base plate using thin aluminum foil (2 μm), sandwiched between the two and annealed at 570 °C. Silicon forms a eutectic with aluminum at this temperature, forming a permanent bond. A more detailed discussion on these techniques is presented in Ramaswamy et al. [13] and Ramaswamy [14]. Structures with different channel size and pitch were used in the current study and the geometrical details are listed in Table 1.

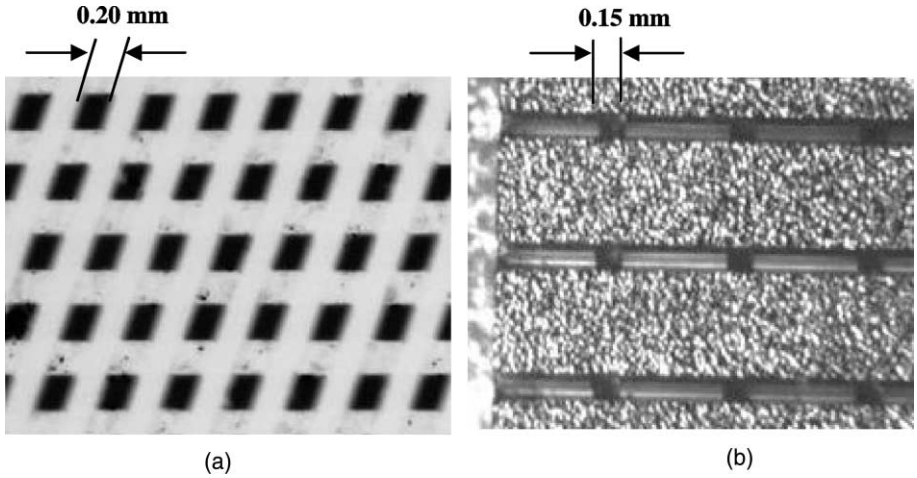

Fig. 3. Top view of microfabricated enhanced structures (a) wet-etched (b) wafer-diced.

Table 1
Enhanced structures employed in the visualization

Structure identification number	Channel width, W_t (mm)	Channel pitch, P_t (mm)	Channel height, H_t (mm)	Thickness of structure, H_s (mm)
S-0.20-1.0-W	0.20	1.0	0.26	0.50
S-0.20-0.7-D	0.20	0.7	0.26	0.51
S-0.15-1.4-D	0.15	1.4	0.26	0.51
S-0.15-0.7-D	0.15	0.7	0.26	0.51
S-0.12-0.7-D	0.12	0.7	0.26	0.51

D: wafer dicing; W: wet chemical etching.

3. Experimental set-up

A schematic of the test facility is shown in Fig. 4. The test set-up consists of evaporator and condenser sections separated by flexible poly-fluoro-alkoxy tubing with an internal diameter of 3.2 mm. This provides a thermosyphon loop with the condenser placed at a higher elevation compared to the evaporator for liquid return by gravity. Fig. 4 also shows a detailed sketch of the evaporator section. The evaporator consists of a plexiglass enclosure (12.7 mm thick walls) of outside dimensions 50 mm × 50 mm × 40 mm. The heater assembly consists of an Omega cartridge heater embedded

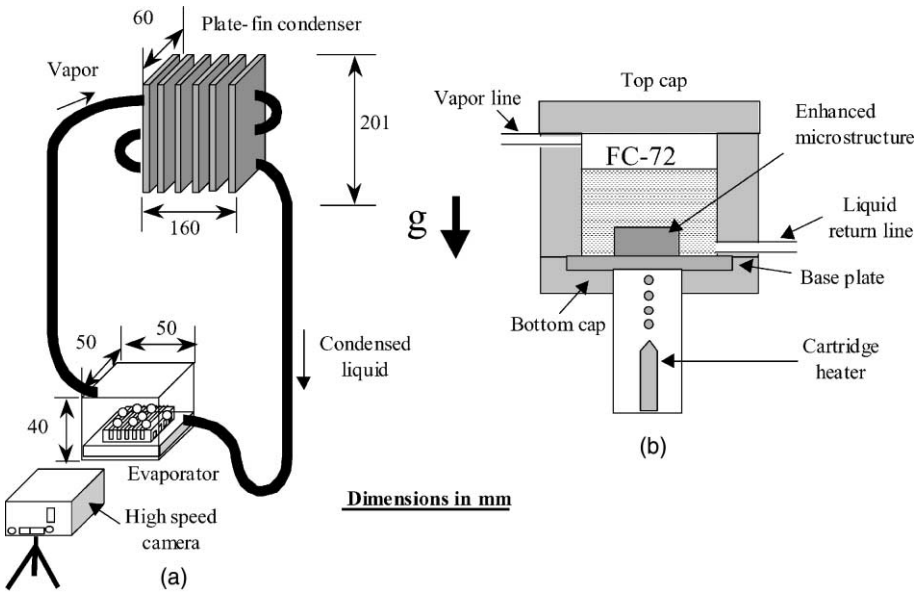

Fig. 4. Schematic of the experimental set-up (a) thermosyphon loop, (b) detailed view of the evaporator section.

into a square copper rod (1.1 cm^2 cross-sectional area). Omegatherm® "201" high thermal conductivity, high temperature paste was applied between the heater and the copper rod for good contact. The copper rod was insulated with plexiglass and additional styrofoam insulation to minimize heat loss. The enhanced structure was soldered to one end of this heater assembly.

Four copper–constantan sheathed thermocouples (0.08 mm diameter) were embedded at the center of the copper rod starting from 4 mm below the boiling surface at intervals of 4 mm. These thermocouples were used to calculate the heat flux at the base of the enhanced structure (1 cm^2) by a one-dimensional heat conduction analysis. Pool temperature in the evaporator section was measured using an embedded copper–constantan thermocouple of 0.08 mm diameter. The thermocouple measurements were acquired using a National Instruments data acquisition system interfaced to a personal computer and controlled using LabVIEW software.

A variac (0–140 V) supplied power to the heater. Voltage taps were placed on the heater lead wires very near the sheath. This provided precise measurement of voltage drop across the heater. A precision resistor ($1 \pm 0.01\ \Omega$) was connected in series to the power supply to measure the line current. A Fluke 87 True RMS multimeter measured the voltages.

A plate fin condenser was employed with the fin spacing of 6 mm optimized for operation in natural convection. A Robinair pressure gauge (−101 kPa to 0.8 MPa) was attached to the loop near the exit of the condenser to monitor the loop pressure during operation and during leak test of the set-up (in vacuum and under pressure). An ice cooled spiral tube reflux condenser was used to trap any vapor leaving the condenser. It also provided a vent for the system to maintain it at atmospheric pressure throughout the tests.

The flow visualization set-up consisted of a high-speed CCD camera (model—Phantom) capable of frame rates up to 1600 frames/s with a split field. The CCD image size was 512 pixels across by 512 pixels. With an aspect ratio of 1:1 a maximum of 500 frames/s was captured. Setting the aspect ratio to 2:1 gave two subfields for each normal field, allowing two times the number of images (of half the height). This resulted in 1000 images of 512 pixels across by 256 pixels (at the same 500 frames/s speed). The camera had a personal computer integrated into it, which was used to control the capturing and storing of images. The camera vendor (Vision Systems, Inc.) supplied the front-end software, which was used to control the capture sequence. The input parameters were speed of capture, number of frames to store after triggering the capture and the aspect ratio of the image. An instant replay allowed reviewing the captured images in slow motion.

A zoom lens (Navitar 6000) was used to magnify the area of interest and work at close distances to the boiling structure. The lens was capable of a variable magnification of 1–6.5 times the original size of the object. A 150 W fiber optic light guide was used for illuminating the structure.

4. Experimental procedure

Every experimental run was preceded by a degassing operation. The vent valve was opened and a heat input of 70 W was supplied to the heater (to start vigorous boiling). Boiling was sustained for about 1 h and then the system was allowed to cool down for 2 h. The vent valve was kept closed during this period. The system reached room temperature by this time in all the runs. Before commencement of the test runs, the valve was again opened to ensure atmospheric conditions inside the system at all heat input levels. This procedure ensured that the dissolved gas concentration of non-condensibles was uniform, if not zero, in all the runs.

The initial heat input was set at 1 W and incremented in steps of 1 W until boiling was observed. Subsequently, the increments were increased to 2.5 W. The image capture was carried out along with the temperature measurements. For each value of power input, the system was allowed to reach steady state (defined by a rise of less than 0.2 °C in a span of 10 min). The image capture software was used to start the capture and 500 images were acquired sequentially at a speed of 1500 frames/s (4:1 aspect ratio). The capture sequence was replayed and the number of images to be stored adjusted to capture at least 10 cycles of bubble growth and departure. The images were then transferred to permanent storage on the computer. The temperatures were then recorded at two-second intervals for 1 min. The averaged values were used to calculate the temperature gradient and the heat input. The voltages across the heater and the precision resistor were recorded during the data acquisition and used to calculate the electrical input to the system.

This procedure was repeated at each heat flux until the liquid inside the evaporator was agitated so vigorously (because of bubble generation) that the captured frames did not provide any meaningful pictures. The magnification was kept fixed for each experimental run (depending on the channel size). The images were analyzed using the image analysis software provided by the camera vendor (Phantom) and the parameters measured were bubble departure diameter, frequency and growth period. The nucleation site density was measured by direct observation.

5. Measurements and uncertainty analysis

The thermocouples and the data acquisition system were calibrated against a precision mercury thermometer

at ice point to an uncertainty of ±0.1 °C. The uncertainty in voltage measurement was specified by the manufacturer as ±0.7% of the reading. The precision resistor used to measure the line current was accurate to ±1%. Uncertainty estimates for the derived quantities were made using the Kline and McClintok [15] technique. The uncertainty in the wall superheat values was ±0.12 °C. As a result of the linear curve fit of the temperature data, from the inline thermocouples, the maximum uncertainty in the heat flux was ±13.6%.

For the flow visualization studies, the maximum uncertainty in measuring the bubble diameters was ±23% at initiation of the bubble growth and ±7.8% at departure. The uncertainty in frequency measurement was estimated as ±3.5% and for the nucleation site density it was ±11.2%.

6. Experimental results

6.1. Boiling regimes

Zuber [16] classified boiling from plain surfaces into several regimes. The first of these was termed 'laminar'. In this regime, the bubbles are intermittently formed at active cavities. Each bubble maintains its identity from formation to departure. The second regime was termed as 'turbulent' where a few bubbles merge with their predecessors. Hence there is some amount of vertical coalescence. In the third regime almost all bubbles coalesce with their predecessors and vapor columns are formed at the active cavities. This regime eventually ends up with two or more vertical columns combining to form a larger mushroom cloud above the boiling surface.

The current observations show that boiling from enhanced structures has some similarity. At low wall superheat values (4–7 °C), bubbles maintaining distinct identities were generated from the active pores at a constant rate (Fig. 5a). However, the wake from a departing bubble did exert a pulling force on its successor. With a rise in the wall superheat values (up to 12 °C), the number of active sites increased and at some sites vertical coalescence was observed. The formation of vapor columns at the active sites, beyond this point, depended on the pore pitch. For structures with a large pore pitch (e.g. 'S-0.15-1.4-D') vapor stems were formed similar to the observation of Zuber [16] before leading to a mushroom cloud. However, as the pitch was reduced (e.g. 'S-0.15-0.5-W' and 'S-0.2-0.5-W'), the bubbles coalesced laterally before vertical coalescence occurred. Hence the spacing of the pores defines the coalescence mechanism to some extent, unlike in plain surfaces where it is a random event. For all the structures, at high wall superheats (20–30 °C), large mushroom clouds were formed (Fig. 5b). Hence in this range the enhanced structures seem to behave like a plain surface.

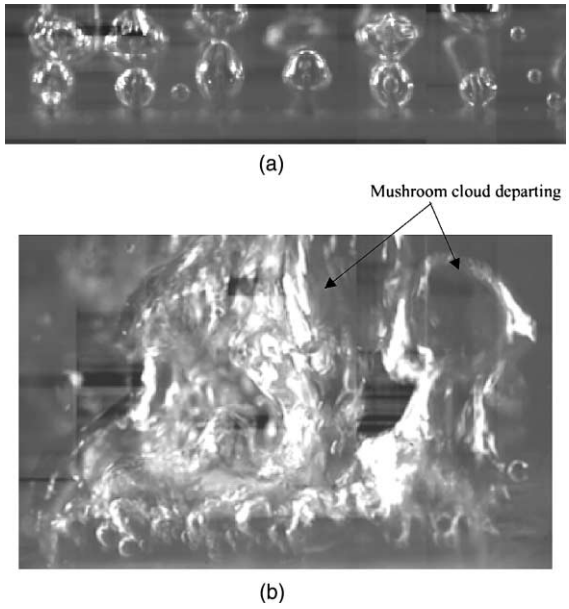

Fig. 5. (a) Isolated bubble regime (laminar regime) for boiling from structure 'S-0.15-1.4-D', $\Delta T_{sup} = 7.3$ °C, (b) mushroom cloud formation at high wall superheat values (25–30 °C) for structure 'S-0.2-1.0-W'.

The experiments conducted by Chien and Webb [11] were all in the isolated bubble regime (laminar regime). For this regime, a switching mechanism was observed where some of the active pores suddenly become inactive and some inactive pores become active. This phenomenon was observed in the current study for structures with larger pores only ($D_p = 200$ μm). For the other pore sizes, the active pores remained active throughout the experiments. Chien and Webb [11] also observed that the bubbles departing from the same pore did not have a constant diameter. A similar observation was made in the current study. In addition, the bubbles from different pores also displayed a size distribution. Hence a large sample of bubbles was collected, in this study, to arrive at a mean departure diameter.

6.2. Bubble departure diameter

A still picture of the structure was taken at the beginning of each experiment. Using this as the reference image, the conversion factor from pixels to mm was first evaluated. The video sequence was played frame by frame and the diameter measured for the frame where the bubble departed from the pore. As mentioned in the previous section, the bubble diameter varied from the same pore and between different pores. Hence a large sample size (~50 bubbles) was taken to arrive at a mean departure diameter. The bubble departure diameters were found to fit a normal distribution. A few examples

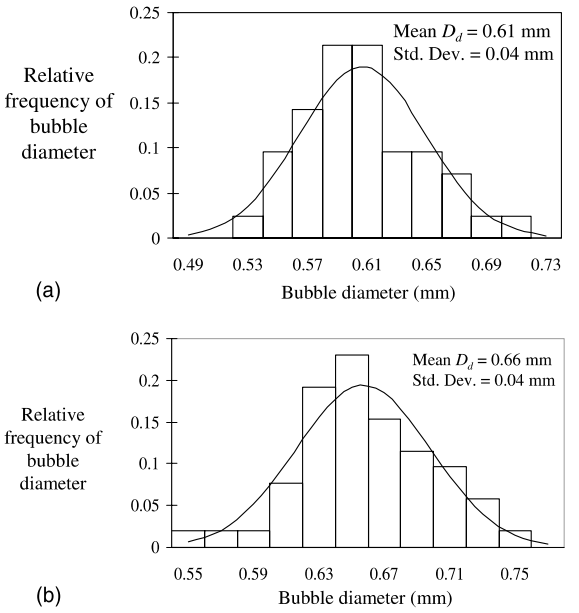

Fig. 6. Distribution of bubble departure diameter (a) S-0.2-0.7-D, $\Delta T_{sup} = 4.8$ °C, (b) S-0.15-1.4-D, $\Delta T_{sup} = 12.3$ °C.

are shown in Fig. 6. The average values were then plotted as a function of the wall superheat (Fig. 7).

The results show that the bubble diameters increase with an increase in the wall superheat values. The studies by Nakayama et al. [9] and Chien and Webb [11] show an opposite trend where the bubble departure diameter reduced with increase in the wall superheat. Kolev [17] developed a bubble departure model for boiling on plain surfaces. The model shows that the bubble diameters reduce with increasing wall superheat in the range of 0–3 °C. Beyond 3 °C, the values start increasing and this trend continues up to ~20 °C. After this the bubble diameter again starts decreasing very sharply. Recently, Fournelle et al. [18] conducted flow visualization on isolated reentrant cavities etched on a silicon surface. Their study also shows that in the range 5–30 °C, the departure diameter increases with an increase in the wall superheat. Zuber [16] suggested that for very low wall superheats the bubble departure is a function of the buoyancy and surface tension forces only. With an increase in the wall temperature, the surface tension reduces (for most fluids). This would result in a decrease in the departure diameter. However, as the wall superheat is increased further, dynamic forces (e.g. inertia forces) start dominating the bubble growth and hence the bubble diameter shows an increasing trend with increase in wall superheat.

In addition to the above observation, the current study shows that for a fixed pore size the pore pitch very weakly influences the bubble diameter. For a fixed pore pitch, a larger pore resulted in a larger departure diameter.

6.3. Frequency measurement

To measure frequency, a sample size of at least 10 bubbles was used. The time elapsed from the beginning of the first bubble growing to departure of the 10th bubble was measured and the average time for one bubble cycle evaluated. This was done for at least 10 sequences and once again an average value of frequency calculated.

The results for average frequency as a function of the wall superheat are shown in Fig. 8. The frequency of bubble generation increased initially with an increase in the wall superheat. However, at intermediate wall superheats (8–12 °C), the frequency actually decreased. At low wall superheat values (4–6 °C), the bulk liquid in the evaporator was nearly stationary similar to pool boiling and the departing bubbles did not get affected by the liquid flowing in from the return line. However, with an increase in the wall superheat, the liquid returning into the evaporator induced a sweeping motion on the

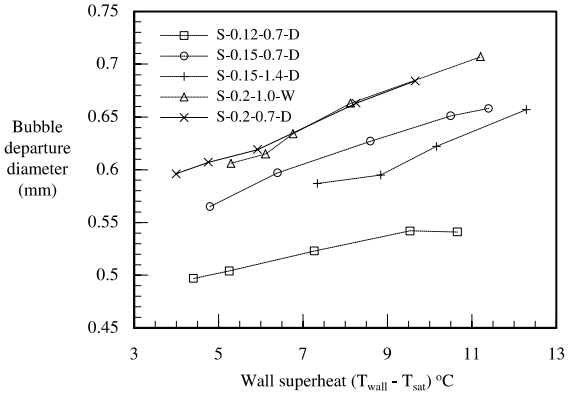

Fig. 7. Average bubble departure diameter vs. wall superheat.

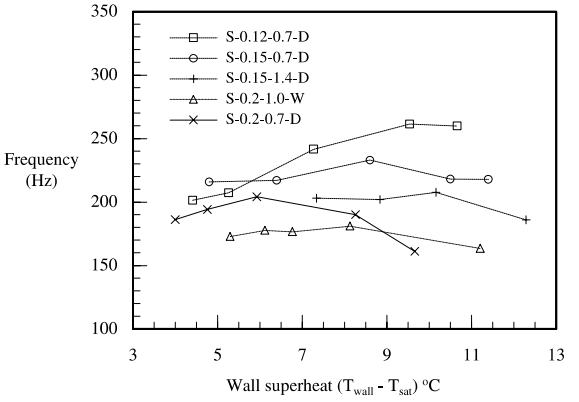

Fig. 8. Average frequency vs. wall superheat.

enhanced structure. This process was observed to be random and inhibited bubble generation for brief periods of time. It is hypothesized that for boiling in large volumes of liquid, this decrease in frequency might not occur.

The results also show that the frequency of bubble generation reduces with an increase in the pore diameter or the pore pitch. It is attempted to interpret these findings on the basis of dynamic modeling of the events. More details are presented in an accompanying paper that describes the semi-analytical model [19].

6.4. Growth rate

The process of bubble generation in the isolated bubble regime is intermittent. In this regime, a bubble cycle typically consisted of three phases—waiting phase, growth phase and an intake phase. The growth period was measured by replaying the cine sequences frame by frame and monitoring approximately 10 bubbles from the point where they protrude from the pores until they depart. An average growth period was then evaluated. The liquid intake period was less than the resolution of the camera and is assumed to be much smaller than the waiting and growth periods. The waiting time was then evaluated using the following equation.

$$\Delta t_w = f^{-1} - \Delta t_g \quad (1)$$

Sample pictures of a bubble cycle (from beginning to end) are shown in Fig. 9. The instantaneous bubble diameters were plotted as a function of time. Two cases are presented in Fig. 10. The results show a nearly linear growth rate. The growth rate from plain surfaces is usually divided into two phases—an inertia driven phase where the bubble initiation takes place, and a heat transfer controlled phase where the bubble grows [20]. The inertia driven phase is typically significantly smaller than the heat transfer controlled phase and most studies

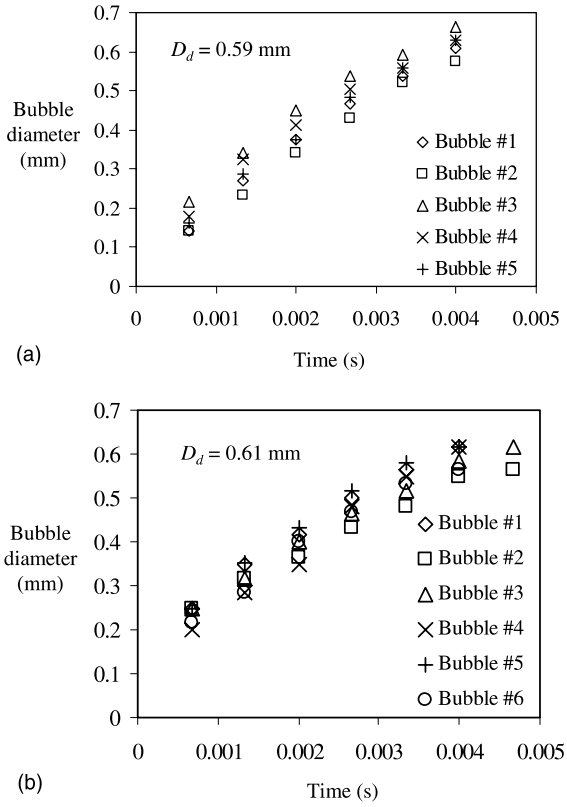

Fig. 10. Instantaneous bubble diameters (a) 'S-0.15-1.4-D', ΔT_{sup} = 7.3 °C, (b) 'S-0.2-1.0-W', ΔT_{sup} = 5.3 °C.

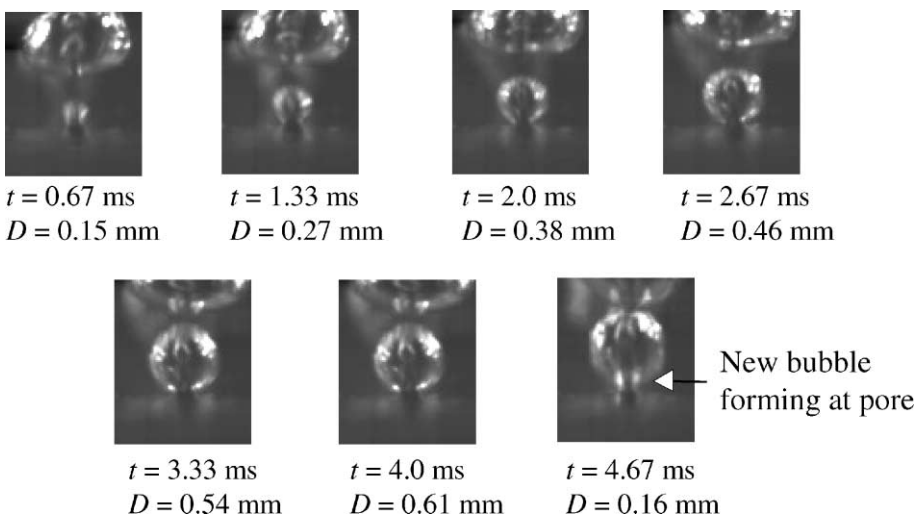

Fig. 9. Bubbles growing at a pore for structure S-0.15-1.4-D, ΔT_{sup} = 7.3 °C.

assume that the entire growth period is heat transfer controlled. For the inertia driven phase, the instantaneous diameter varies linearly with time. On the other hand, for the heat transfer controlled regime, the variation is proportional to the square root of time. The current study shows that the mechanism of bubble growth is indeed different from that on plain surfaces and is inertia driven for the entire growth period (linear with time). This confirms the findings of Chien and Webb [11] who made a similar observation with their structured surface.

6.5. Nucleation site density

The number of bubbles generated on the surface was calculated by direct observation. Since the pores on all the structures were on a square grid, the number of bubbles generated at the outermost rows (or columns) shadowed the ones generated at the center. Hence an approximate method was used to calculate the number of bubbles. The number of bubbles on the outermost rows was first recorded (by viewing the front and back of the structure). An average value was thus calculated for number of bubbles generated per row. Next, the number of active rows was recorded by viewing the structure from the sides (left and right). The total number of bubbles was evaluated by multiplying the two numbers. The nucleation site density was evaluated by dividing the number of bubbles generated by the external surface area of the structure.

The resulting nucleation site density is plotted as a function of wall superheat in Fig. 11. The results show that the number of bubbles formed increases with an increase in the wall superheat. For plain surfaces, this phenomenon occurs because sites with larger cavity sizes get activated with an increase in wall superheat. For the structured surfaces, the cavity size is fixed (by the pore size) and hence the increase in number of bubbles occurs because of an increase in the amount of liquid evaporated in the tunnels.

The results also show that as the pore pitch was increased, the nucleation density decreases. With an increase in the pitch, the number of pores on the surface is reduced and hence the nucleation density is also smaller.

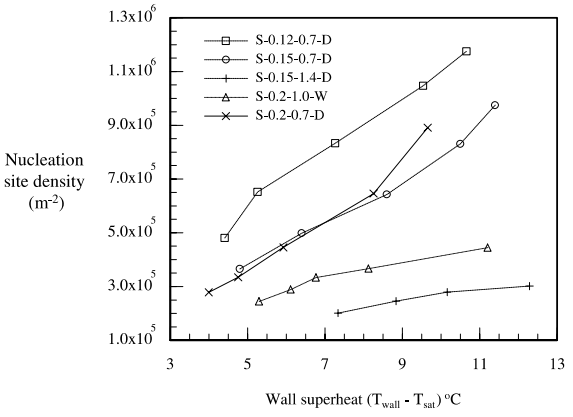

Fig. 11. Nucleation site density vs. wall superheat.

7. Framework for semi-analytical model

A semi-empirical model for prediction of heat transfer rates from the enhanced structure was developed that used the bubble data recorded above. Fig. 12 shows how the measured data and the other boiling parameters feed into each other to form a semi-analytical model. Sub-models for the bubble departure diameter, frequency and nucleation site density have been developed in conjunction with a correlation for liquid evaporation inside the channels [19]. The semi-analytical model predicts the total heat transfer rate at a certain wall superheat.

Fig. 13 shows the comparison between measured data and prediction based on this model, for a few structures (Table 2). The predicted results for heat flux are within ±30% of the experimental ones. Details on prediction accuracy of the sub-models are included in the accompanying paper [19]. Accurate prediction of the evaporation inside the channels seems to be the most dominant factor in the efficacy of the model.

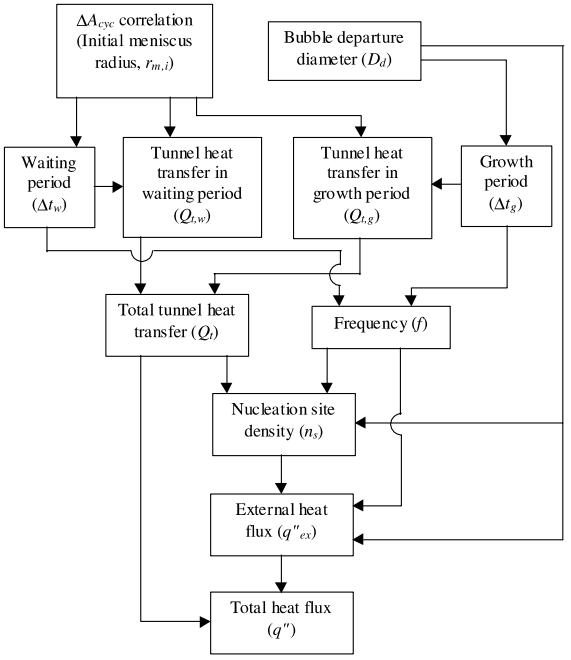

Fig. 12. Schematic of the semi-analytical model showing the various components and their interdependency.

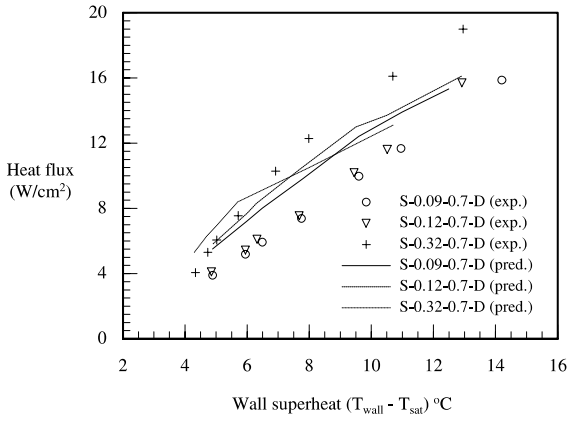

Fig. 13. Comparison of predicted and experimental heat flux (structures S-0.09-0.7-D, S-0.12-0.7-D and S-0.32-0.7-D).

Table 2
Geometrical details of enhanced structures in Fig. 13

Structure identification number	Channel width, W_t (mm)	Channel pitch, P_t (mm)	Channel height, H_t (mm)	Thickness of structure, H_s (mm)
S-0.09-0.7-D	0.09	0.7	0.26	0.51
S-0.12-0.7-D	0.12	0.7	0.26	0.51
S-0.32-0.7-D	0.32	0.7	0.26	0.51

D: wafer dicing.

8. Conclusions

A flow visualization study was conducted to understand the mechanism of boiling from enhanced structures in the wall superheat range 4–30 °C. The following conclusions were drawn based on the study:

(a) There are distinct boiling regimes for enhanced structures similar to that for plain surfaces. For low to intermediate wall superheat values (4–12 °C), the boiling was in the isolated bubble regime. With an increase in the wall superheat, coalescence occurs, leading eventually to formation of mushroom clouds. The coalescence phenomenon was controlled to some extent by the pore pitch.
(b) The average bubble departure diameter increased with an increase in the pore size (for same wall superheat). The effect of pore pitch was very small. For a certain pore size, the departure diameter increased with an increase in the wall superheat.
(c) The frequency of bubble generation increased marginally with an increase in the wall superheat. At intermediate wall superheats (~12 °C), the frequency showed a decreasing trend. This decrease might be a manifestation of the induced flow inside the compact evaporator. It is hypothesized that for large pools this reduction will not be observed. The frequency reduced with an increase in the pore pitch and pore diameter.
(d) The nucleation site density increased with an increase in the wall superheat (for all structures). A larger pitch resulted in fewer bubbles because of fewer pores. The pore size had negligible effect except for one structure where the number of bubbles increased. The nucleation site density is a function of the volume evaporated inside the tunnels and the average departure diameter of the bubbles. With a change in the pore size, interplay of these two parameters leads to reduction/no change/increase in the nucleation site density.

Acknowledgements

This work was performed while the authors were at the University of Maryland, College Park. The authors would like to acknowledge support of this work through the members of CALCE Electronic Products and Systems Center and the Defense Advanced Research Projects Agency contract N00164-99-C-0039 and Semiconductor Research Corporation contract 99-NJ-649. We also thank Professor Jim Duncan, at the University of Maryland, for providing us with the high-speed visualization equipment. We thank Professor John Melngailis and his staff for providing us access to the cleanroom and assisting us in fabricating the enhanced structures.

References

[1] C.Y. Han, P. Griffith, The mechanism of heat transfer in nucleate pool boiling, Int. J. Heat Mass Transfer 8 (1965) 887–914.
[2] D.D. Paul, S.I. Abdel-Khalik, A statistical analysis of saturated nucleate boiling along a heated wire, Int. J. Heat Mass Transfer 26 (1983) 509–519.
[3] C.N. Ammerman, S.M. You, Identification of pool boiling heat transfer mechanisms from a wire immersed in saturated FC-72 using a single-photo/LDA method, J. Heat Transfer 118 (1996) 117–123.
[4] K.-H. Sun, J.H. Lienhard, The peak boiling heat flux on horizontal cylinders, Int. J. Heat Mass Transfer 13 (1970) 1425–1439.
[5] Y. Katto, S. Yakoya, Behavior of a vapor mass in saturated nucleate and transition boiling in pool boiling, Heat Transfer—Japanese Res. 5 (1976) 45–65.
[6] R.L. Webb, Principles of Enhanced Heat Transfer, John Wiley & Sons, New York, 1994.
[7] W. Nakayama, T. Daikoku, H. Kuwahara, T. Nakajima, Dynamic model of enhanced boiling heat transfer on porous surfaces, part I: experimental investigation, J. Heat Transfer 102 (1980) 445–450.

[8] W. Nakayama, T. Daikoku, H. Kuwahara, T. Nakajima, Dynamic model of enhanced boiling heat transfer on porous surfaces, part II: analytical modeling, J. Heat Transfer 102 (1980) 451–456.
[9] W. Nakayama, T. Daikoku, T. Nakajima, Effects of pore diameters and system pressure on saturated pool boiling heat transfer from porous surfaces, J. Heat Transfer 104 (1982) 286–291.
[10] J. Arshad, J.R. Thome, Enhanced boiling surfaces: heat transfer mechanism and mixture boiling, in: Proceedings of ASME-JSME Thermal Engineering Joint Conference, vol. 1, 1983, pp. 191–197.
[11] L.-H. Chien, R.L. Webb, Measurement of bubble dynamics on an enhanced boiling surface, Exp. Thermal Fluid Sci. 16 (3) (1998) 177–186.
[12] W. Nakayama, T. Nakajima, S. Hirasawa, Heat sink studs having enhanced boiling surfaces for cooling microelectronic components, ASME Paper No.84-WA/HT-89, 1984.
[13] C. Ramaswamy, Y. Joshi, W. Nakayama, W.B. Johnson, Compact thermosyphons employing microfabricated components, Microscale Thermophys. Eng. 3 (4) (1999) 273–282.
[14] C. Ramaswamy, A compact two-phase thermosyphon employing microfabricated boiling enhancement structures, Ph.D. Thesis, University of Maryland, College Park, MD, 1999.
[15] S.J. Kline, F.A. McClintock, Describing uncertainties in single sample experiments, Mech. Eng. 75 (1953) 3–8.
[16] N. Zuber, Nucleate boiling—the region of isolated bubbles—similarity with natural convection, Int. J. Heat Mass Transfer 6 (1963) 53–56.
[17] N.I. Kolev, The influence of mutual bubble interaction on the bubble departure diameter, Exp. Thermal Fluid Sci. 8 (1994) 167–174.
[18] G. Fournelle, S.H. Bhavnani, R.C. Jaegar, Optical Study of Enhanced Heat Transfer from a Heat Sink for Microelectronic Applications, in: D. Agonafer, M. Saka, Y.-C. Lee (Eds.), Advances in Electronic Packaging,, EEP-Vol. 26-2, 1999.
[19] C. Ramaswamy, Y. Joshi, W. Nakayama, W.B. Johnson, Semi-analytical model for boiling from enhanced structures, Int. J. Heat and Mass Transfer, submitted for publication.
[20] B.B. Mikic, W.M. Rohsenow, A new correlation of pool-boiling data including the effect of heating surface characteristics, J. Heat Transfer 91 (1969) 245–250.